Journal of Rock Mechanics and Geotechnical Engineering 18 (2026) 3526–3538

Contents lists available at ScienceDirect

Journal of Rock Mechanics and Geotechnical Engineering

journal homepage: www.jrmge.cn

Full Length Article

Independence verification of peak-strength strain energy storage index from rock specimen shape effects

Zhichao He [a], Fengqiang Gong [a,b,*], Li Ren [b,**], Da Huang [c], Weimin Yang [d]

[a] School of Civil Engineering, Southeast University, Nanjing, 211189, China
[b] State Key Laboratory of Intelligent Construction and Healthy Operation and Maintenance of Deep Underground Engineering, Sichuan University, Chengdu, 610065, China
[c] School of Geological Engineering and Geomatics, Chang'an University, Xi'an, 710064, China
[d] School of Qilu Transportation, Shandong University, Ji'nan, 250002, China

ARTICLE INFO

Article history:
Received 5 January 2025
Received in revised form
2 July 2025
Accepted 15 July 2025
Available online 15 September 2025

Keywords:
Rock mechanics
Rockburst
Strain energy storage index
Linear energy storage (LES) law
Energy storage coefficient
Peak-strength strain energy storage index

ABSTRACT

The strain energy storage index (W_{ET}) is a crucial index for evaluating rockburst proneness. Interestingly, when conducting tests to obtain W_{ET}, variations exist in the shape of coal or rock specimens. However, whether shape factors affect W_{ET} has not been theoretically and experimentally verified. In this study, to investigate the independence of W_{ET} from specimen shape effects, its rationality was first theoretically derived based on the linear energy storage (LES) laws of rock, indicating that W_{ET} is influenced by the energy storage coefficient (ESC) of the rock. Two typical rock materials (granite and red sandstone) with different rockburst proneness were selected to verify the migration effect of cubic and cylindrical specimens on W_{ET} via uniaxial compression tests. The experimental results revealed that the mechanical behavior characteristics of rocks were affected by the shape of cylindrical and cubic specimens, whereas the W_{ET} and ESC were opposite. Furthermore, the practical W_{ET} values closely approximate the theoretical values of energy storage-dissipated ratio predicted by the LES law, converging to the peak-strength strain energy storage index (W_{ET}^{P}). Based on the LES law, the influence of specimen shape on W_{ET} and W_{ET}^{P} was further discussed, concluding that W_{ET} and W_{ET}^{P} are independent of specimen shape effects. Furthermore, the W_{ET}^{P} is more stable than W_{ET} and reflects the relative magnitude of energy storage and dissipation during the entire pre-peak of rock. Thus, the peak-strength strain energy storage index can be used as a substitute for W_{ET} in evaluating the rockburst proneness of rock.

1. Introduction

Rockburst is a dynamic geological disaster caused by the sudden release of elastic strain energy in rock masses, posing serious risks to deep engineering projects and the safety of personnel and equipment (Cook, 1963; Panthi, 2012; Cai, 2016; Feng et al., 2017; Afraei et al., 2018; Keneti and Sainsbury, 2018; Askaripour et al., 2022; Gong et al., 2023; He et al., 2023; Dai et al., 2025; Li, et al., 2025a, 2025b; Luo et al., 2025; Si et al., 2025; Zhang et al., 2025). Rockburst proneness evaluation is crucial for analyzing and predicting potential rockburst disasters (Kidybiński, 1981; Wang and Park, 2001; Cai, 2016; Gong et al., 2020, 2022a; He et al., 2025a, 2025b; Xu et al., 2025a, 2025b; Ran et al., 2025a, 2025b). The strain energy storage index (W_{ET}) is widely utilized in deep engineering to assess the rockburst proneness of coal or rock (Peng, 1978; Kidybiński, 1981; Tan, 1992; Brauner, 1994; Wang and Park, 2001; Shan and Yan, 2010; Zhao and Jiang, 2010; Yang et al., 2018; He et al., 2021b). The W_{ET} was initially proposed by Neyman et al. (1972) and Szecowka et al. (1973) as an energy index to evaluate the burst tendency of coal. Kidybiński (1981) further developed this index, which led to the currently recognized calculation method of W_{ET} and established an initial classification standard. The specific calculation method is illustrated in Fig. 1.

* Corresponding author. School of Civil Engineering, Southeast University, Nanjing, 211189, China.
** Corresponding author.
E-mail addresses: gongfengqiang@seu.edu.cn, fengqiangg@126.com (F. Gong), renli@scu.edu.cn (L. Ren).
Peer review under responsibility of Institute of Rock and Soil Mechanics, Chinese Academy of Sciences.

https://doi.org/10.1016/j.jrmge.2025.07.005

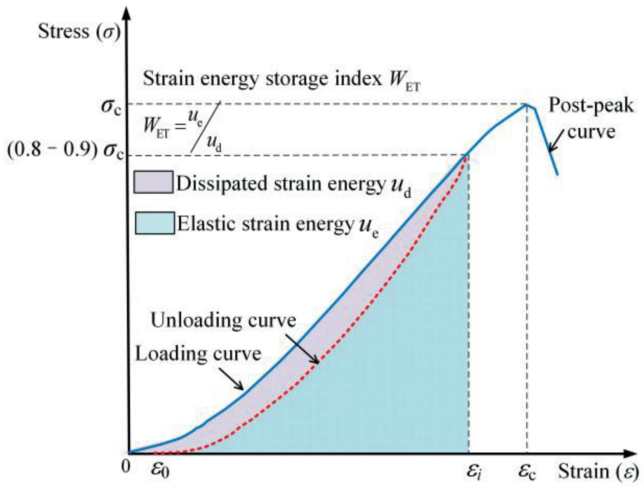

Fig. 1. Scheme of strain energy parameters used to calculate W_{ET} (σ_c: Peak strength, ε_i: Strain at (0.8-0.9)σ_c unloading, ε_0: Residual strain).

Since the calculation principle and process of W_{ET} are relatively simple and accurate, it is not only utilized to evaluate the bursting proneness for coal, but is also frequently employed to determine the rockburst proneness of rock. In 1988, Singh (1988) adopted W_{ET} as an evaluation index for rockburst proneness of hard rock. The higher W_{ET}, the greater the elasticity and rigidity in brittle rock. Consequently, more energy accumulates in the rock before failure, increasing the likelihood of rockbursts occurring during failure and the severity of resulting rockbursts. Stewarski (1987) introduced the rock dynamic index that is determined by the same ratio of the W_{ET} index, but for a loading test on a split Hopkins pressure bar. Singh (1988) proposed the burst energy release index (BERI), which represented the energy released at the time of rock fracture, and noted an increase in BERI with an increase in W_{ET}. Some scholars have employed artificial intelligence or numerical simulation methods to demonstrate the validity of using the W_{ET} index for predicting rockburst proneness (Dong et al., 2013; Zhou et al., 2016, 2018; Afraei et al., 2018; Li and Jimenez, 2018; Ahmad et al., 2022; Khan et al., 2022; Qu et al., 2022; Wang et al., 2025). Additionally, Gong et al. (2019a, b) revealed the linear energy storage (LES) laws in which the elastic strain energy increases linearly with the total input strain energy, and proposed the peak-strength strain energy storage index (W_{ET}^{P}). What's more, Gong et al. (2022a) theoretically demonstrated the validity of W_{ET} at a 0.8 stress level based on the LES law of rocks.

On the other hand, the shape and size of the specimen are important influential factors in obtaining W_{ET} in actual indoor experiments. Interestingly, when conducting uniaxial compression (UC) tests to obtain W_{ET}, variations exist in the shape of coal or rock specimens, such as cylinders, cubes, and other geometries. In fact, Kidybiński (1981) initially introduced W_{ET} using 50 mm × 50 mm × 50 mm (length × width × height) cubic coal specimens in UC tests. However, it is now common to use the Φ50 mm × 100 mm cylindrical specimen for conducting UC tests to obtain W_{ET} (Wang and Park, 2001; Su et al., 2013; Xiao et al., 2014; Xue et al., 2016; Leveille et al., 2017; Bacha et al., 2020; Sepehri et al., 2020; He et al., 2021a; Luo and Gong, 2022; Klammer et al., 2023; Malki et al., 2025). The migration effect of changing the specimen shape from cubic to cylindrical for obtaining W_{ET} has not been validated theoretically and experimentally. Moreover, whether the shape of the specimen affects W_{ET} is still an open question. Therefore, two main issues remain unresolved: (a) Can the migration effect of W_{ET} from a cube to a cylinder be theoretically and experimentally validated? (b) Does the specimen shape influence the results of W_{ET} evaluation?

Inspired by previous studies and based on the applicability of W_{ET} independent of specimen shape derived from the LES law of rock, this study aims to theoretically and experimentally verify the W_{ET} migration effect of specimen changing from cube to cylinder, as well as the influence of the specimen shape on W_{ET}. Additionally, two typical rock materials (granite and red sandstone) with different rockburst proneness were selected to verify the impact of cubic and cylindrical specimens on the W_{ET} migration effect. The specimens were processed as cubes (50 mm × 50 mm × 50 mm) and cylinders (Φ50 mm × 100 mm). Through UC and SCLUC (single-cyclic loading-unloading uniaxial compression) testing of specimens, the mechanical behavior and strain energy evolution of four types of rock specimens were determined. At the same time, we compared W_{ET} and W_{ET}^{P} with the energy storage-dissipation ratio calculated by the LES law to verify the rationality of W_{ET} and its applicability to cube-to-cylinder specimens. Furthermore, the influence of specimen shape and size on the W_{ET} based on the LES law of rock was further discussed.

2. Theoretical verification of W_{ET} independent of specimen shape effects

From the perspective of energy, the deformation or failure of rocks is the combined result of energy input, storage, dissipation, and release (Xie et al., 2009). Previous research by Gong et al. (2019b) has revealed that the internal elastic strain energy (u_e^i), dissipated strain energy (u_d^i), and input strain energy (u_o^i) of rock specimens under uniaxial compression all exhibit linear relationships, representing the LES and linear energy dissipation (LED) laws of rock. The specific fitting function is as follows:

$$u_e^i = Au_o^i + b \tag{1}$$

$$u_d^i = (1-A)u_o^i - b = Cu_o^i - b \tag{2}$$

where the parameters A and C are named compression energy storage coefficient and compression energy dissipation coefficient, respectively. These coefficients effectively reflect the energy storage and dissipation capacity of coal or rock under compression. The b represents a fitting constant.

The calculation method of W_{ET} was mentioned earlier, which is the ratio of u_e^i and u_d^i at 80 %–90 % σ_c from a theoretical point of view. Based on the LES and LED laws, it is evident that the u_e^i and u_d^i of rock specimens increase linearly with the increase in u_o^i. Furthermore, the sum of u_e^i and u_d^i equals the u_o^i. Therefore, by utilizing the LES law and the LED law of rocks, we can derive the theoretical formula for W_{ET}, which can be named the energy storage-dissipation ratio (W_{ET}^i). It can be expressed as follows:

$$W_{ET}^i = \frac{u_e^i}{u_d^i} \tag{3}$$

Substituting Eqs. (1) and (2) into Eq. (3) yields

$$W_{ET}^i = \frac{Au_o^i + b}{Cu_o^i - b} \tag{4}$$

Additionally, it was found that the value of b is three orders of magnitude smaller than A and C (Gong et al., 2019b). Consequently, Eq. (4) can be further simplified to

$$W_{\mathrm{ET}}^{i'}=\frac{Au_{\mathrm{o}}^{i}}{Cu_{\mathrm{o}}^{i}}=\frac{A}{C}=\frac{A}{1-A} \tag{5}$$

From Eq. (5), it can be seen that the $W_{\mathrm{ET}}^{i'}$ is directly related to the A of rock materials. Additionally, Gong et al. (2022b), Luo and Gong (2022), and Yan et al. (2022) have previously investigated the influence of factors such as specimen size, shape, and length-to-diameter ratio on the A. The results showed that these factors do not affect the A of rock. Furthermore, Gong et al. (2022c) found that the A is independent of the loading rate effect. Therefore, it can be indicated through theoretical formulas that the W_{ET} is not affected by specimen shape effects. However, whether the actual results are consistent with the theoretical deductions still needs further verification through laboratory experiments.

3. Experiment description

3.1. Rock specimen preparation and testing setup

Referring to the relevant literature on W_{ET} testing (Xiao et al., 2014; Xue et al., 2016; Leveille et al., 2017; Bacha et al., 2020; Sepehri et al., 2020; Luo and Gong, 2022; Klammer et al., 2023; Malki et al., 2025), UC tests were carried out on cubic and cylindrical rock specimens in this study. Granite and red sandstone were selected for testing, which were from Miluo in Hunan Province and Linyi in Shandong Province, respectively. The granite and red sandstone materials were processed into cubic specimens of 50 mm × 50 mm × 50 mm and cylindrical specimens of Φ50 mm × 100 mm. Both the granite and red sandstone specimens exhibited good integrity and compactness without surface cracks. To minimize the influence of external factors on the testing, specimens of both granite and red sandstone were taken from the same intact rock, and the sides and end surfaces of the specimens were smoothed before testing. The cylindrical granite and red sandstone specimens were named G-CL and R-CL, and the cubic granite and red sandstone specimens were named G-CB and R-CB, respectively. The diagrams of cubic and cylindrical specimens are shown in Fig. 2. And the basic parameter information of the specimens is measured and presented in Table 1.

All the tests in this paper were conducted on the INSTRON 1346 electro-hydraulic servo testing system (Fig. 3), which contains the test loading system, control and data acquisition system, and hydraulic transmission system. During the testing, data acquisition and recording of axial stress and displacement of rock specimens were realized by using the data system and a 2.5 mm displacement extensometer, respectively. Note: Two rigid steel blocks were placed between the machine indenter and rock specimen to reduce or eliminate the end constraint effect. The deformation data were processed after testing to show the true deformation of the specimen. Additionally, a high-speed camera (Fig. 3) was also employed in this study to capture the rockburst process of the rock specimen, capturing 125 images per second.

3.2. Testing procedures and energy calculation methods

The tests were divided into two parts: UC test and SCLUC test. During the tests, the peak strength (σ_{c}) of specimens is first obtained as the estimated σ_{c} for series SCLUC tests by the UC test. Subsequently, SCLUC tests with different unloading stress levels i (i = 0.1, 0.3, 0.5, 0.7, and 0.9) are carried out. The specimen is firstly loaded to the unloading stress level, then unloaded to zero, and lastly reloaded until the rock specimen fails. During the UC test and the SCLUC tests, when the real-time stress applied by the testing machine exceeded approximately 90 % σ_{c} of the rock specimen, the force control loading (1 MPa/s) was switched to a displacement control (0.065 mm/min) mode to avoid the violent impact of the testing machine. Fig. 4a and b shows the loading path of UC and SCLUC tests.

Strain energy parameters (u_{o}^{i}, u_{e}^{i}, and u_{d}^{i}) at different stress levels are determined via the area integral method. Fig. 4c shows the integration area of strain energy parameters (u_{o}^{i}, u_{e}^{i}, and u_{d}^{i}), and the calculation method can be expressed as (Kidybiński, 1981; Xie et al., 2009):

$$\left.\begin{aligned} u_{\mathrm{o}}^{i}&=u_{\mathrm{d}}^{i}+u_{\mathrm{e}}^{i}\\ u_{\mathrm{e}}^{i}&=\int_{\varepsilon_0}^{\varepsilon_i}f_{\mathrm{u}}(\varepsilon)\mathrm{d}\varepsilon\\ u_{\mathrm{d}}^{i}&=\int_{o}^{\varepsilon_i}f(\varepsilon)\mathrm{d}\varepsilon-\int_{\varepsilon_0}^{\varepsilon_i}f_{\mathrm{u}}(\varepsilon)\mathrm{d}\varepsilon \end{aligned}\right\} \tag{6}$$

where u_{e}^{i} represents the elastic strain energy stored inside the rock specimen during loading, mJ/mm^3. u_{d}^{i} represents the expansion of rock cracks, irreversible plastic deformation, and internal damage dissipated strain energy during loading, mJ/mm^3 (The scope of i is 0–1). The $f(\varepsilon)$ and $f_{\mathrm{u}}(\varepsilon)$ are two functions describing the loading and unloading curves respectively; ε_i is the total strain at the unloading point, and ε_0 denotes the permanent strain after unloading. In this study, the values obtained through the graphical integration method actually represent energy density. However, to better characterize the energy evolution behavior of rocks and to avoid potential confusion among readers, we uniformly adopted the term “strain energy” for representation, while retaining the unit mJ/mm^3.

3.3. Peak-strength strain energy storage index ($W_{\mathrm{ET}}^{\mathrm{P}}$)

Many scholars have pointed out that although the W_{ET} is widely recognized as a simple and accurate indicator for assessing the rockburst proneness of coal or rock materials, its unloading level of about 80 %–90 % σ_{c} only reflects the energy storage and dissipation capacity of rock specimens before reaching peak strength (Zhang et al., 2017; Gong et al., 2022a). However, regarding the selection of unloading at 80 %–90 % σ_{c} for calculating the W_{ET} index, existing

Fig. 2. Rock specimen. (a) Schematic diagram of basic dimensions, and (b) Photograph of specimen.

Table 1
Physical and mechanical properties of rock specimen material.

Lithology	Location	Specimen shape	P-wave velocity (m/s)	Density (g/cm^3)	Elastic modulus (GPa)	Peak strength (MPa)
Granite	Miluo, Hunan Province, China	Cylindrical (G-CL)	3201	2.63	32.61	151.0
		Cubic (G-CB)	3164	2.62	30.93	167.2
Red sandstone	Linyi, Shandong Province, China	Cylindrical (R-CL)	2601	2.37	12.86	76.0
		Cubic (R-CB)	2550	2.37	12.76	98.8

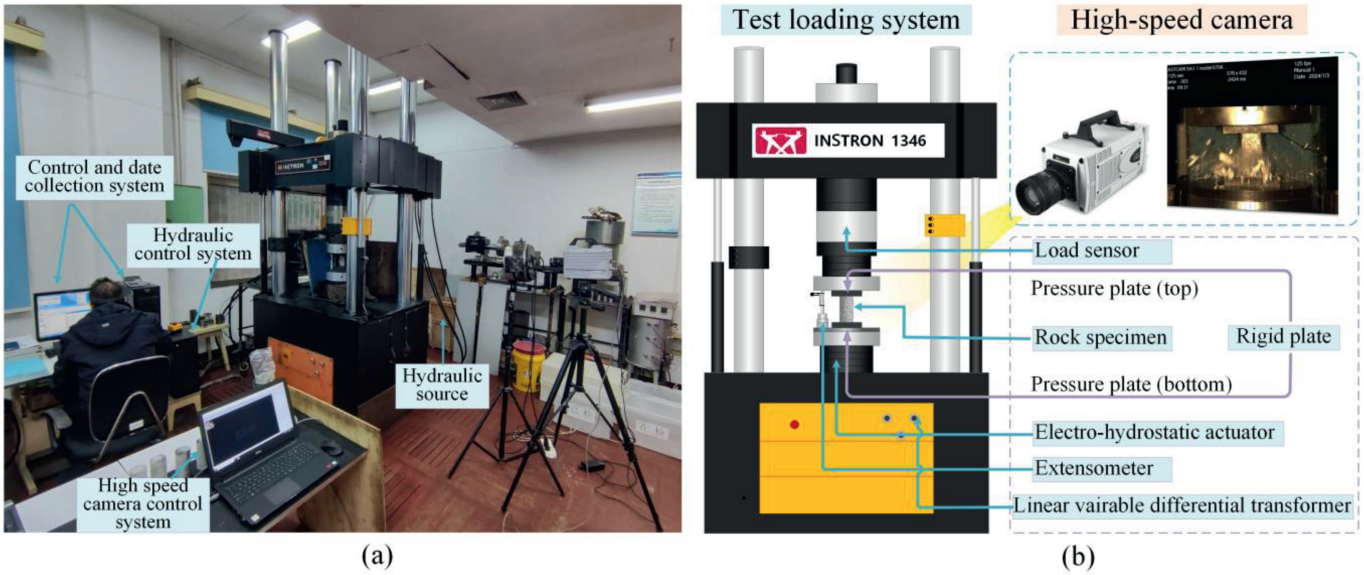

Fig. 3. INSTRON 1346 electro-hydraulic servo testing system. (a) Photograph of the testing system, and (b) Schematic diagram of the testing system.

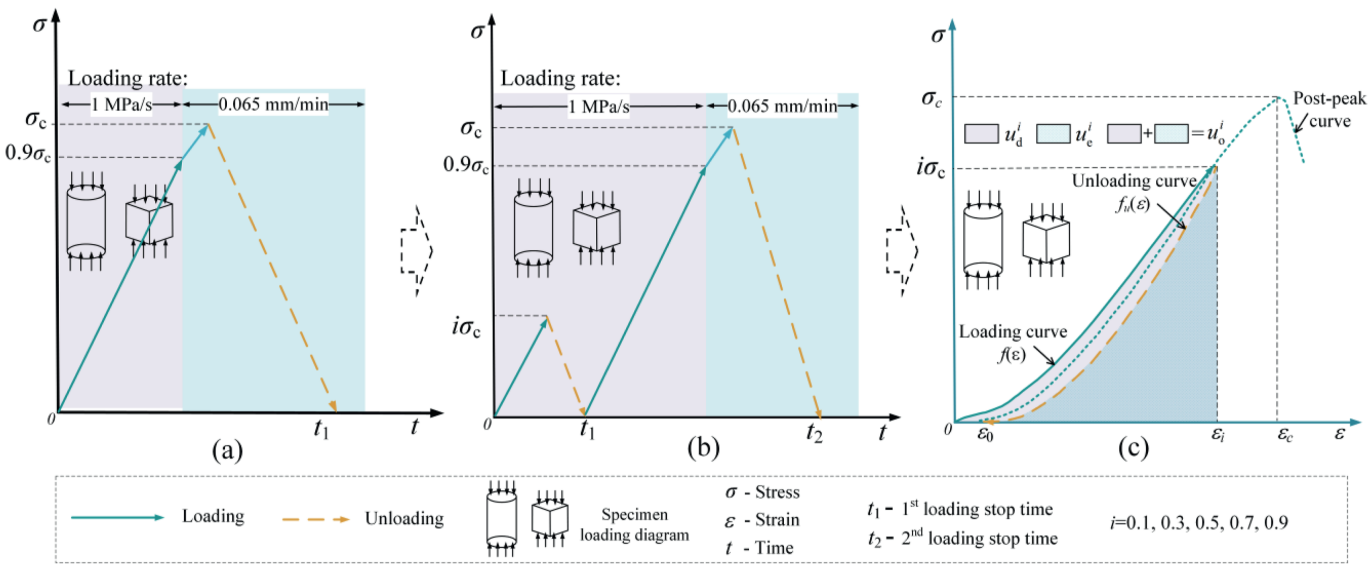

Fig. 4. Schematic diagram of the loading path and the method for determining strain energy parameters in the test. (a) Loading path of the UC test, (b) Loading path of the SCLUC test, and (c) Method for determining strain energy parameters in the SCLUC test.

studies have indicated that this is because unloading at the peak point is difficult to achieve in a timely manner, making it challenging to accurately determine the elastic strain energy at the peak point. In fact, the unloading level for calculating the W_{ET}, closer to the peak strength point, can more accurately reflect the actual energy storage and dissipation capacity of rock specimens when reaching σ_c. In earlier studies, Gong et al. (2019a) realized the accurate calculation of the peak elastic strain energy (u_e^p) of rock specimens based on the discovery of the LES law of rocks, and proposed the W_{ET}^P. The specific calculation of W_{ET}^P is outlined in Eqs. (9) and (10), and the classification criteria for rockburst proneness are provided in Eq. (11).

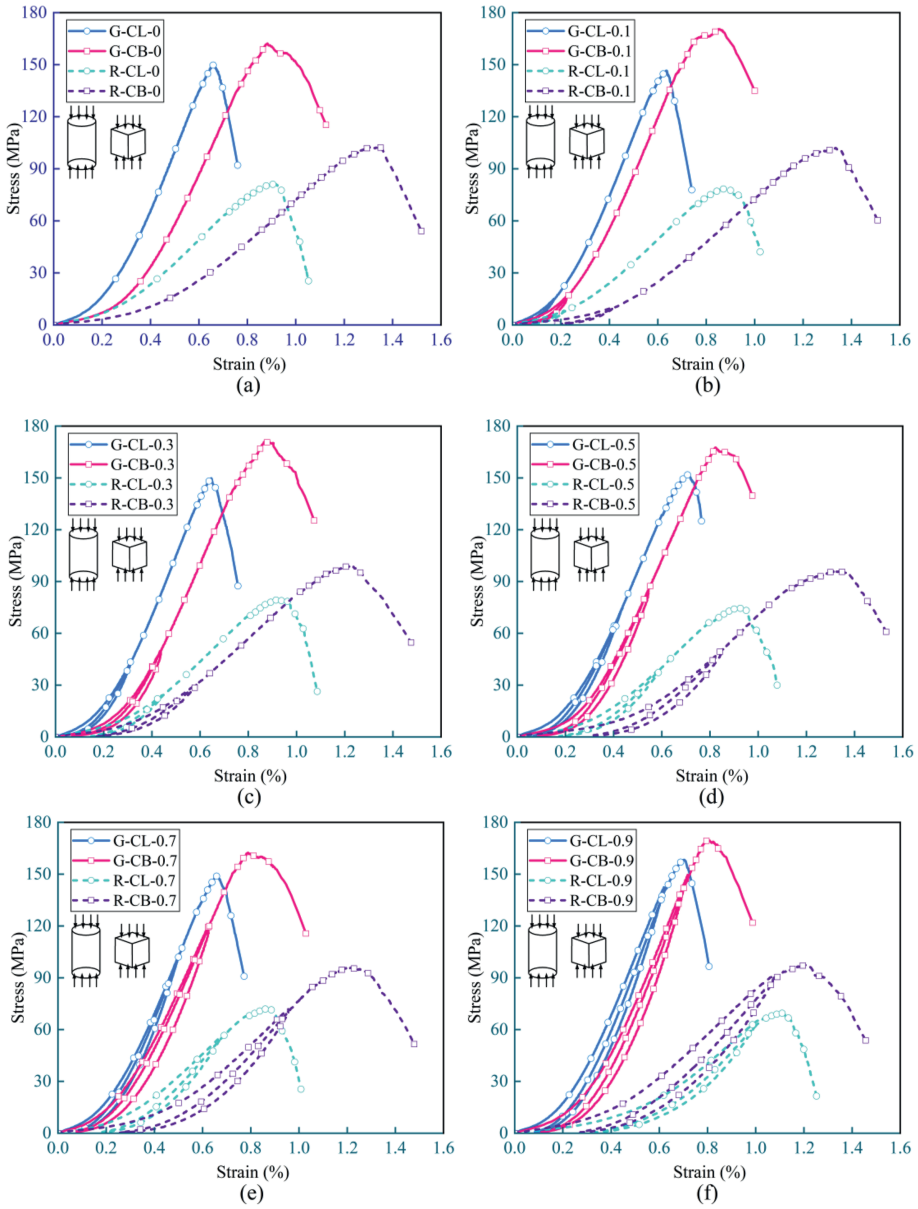

Fig. 5. Stress-strain curves of cylindrical and cubic rock specimens in UC and SCLUC tests. (a) UC test, (b) SCLUC test, $i = 1$, (c) $i = 0.3$, (d) $i = 0.5$, (e) $i = 0.7$, and (f) $i = 9$.

$$u_e^p = Au_o^p + b \tag{7}$$

$$u_d^p = (1-A)u_o^p - b = Cu_o^p - b \tag{8}$$

$$W_{ET}^p = \frac{u_e^p}{u_d^p} \tag{9}$$

$$W_{ET}^p = \frac{Au_o^p + b}{Cu_o^p - b} \tag{10}$$

$$\left.\begin{array}{l} W_{ET}^p > 5 \quad \text{High rockburst proneness} \\ 5 \geq W_{ET}^p \geq 2 \quad \text{Low rockburst proneness} \\ W_{ET}^p < 2 \quad \text{No rockburst proneness} \end{array}\right\} \tag{11}$$

where u_o^p and u_d^p represent the peak input strain energy and peak dissipated strain energy, respectively.

4. Test results and analysis

4.1. Stress-strain curves

Stress-strain curves of cylindrical (G-CL and R-CL) and cubic (G-CB and R-CB) rock specimens under UC and SCLUC tests are shown in Fig. 5. It can be seen that the stress-strain curves of cylindrical and cubic rock specimens under UC and SCLUC tests have undergone initial compaction stage, linear elastic deformation stage, plastic deformation stage, and post-peak failure instability stage. Meanwhile, it can be observed that the evolution trend characteristics of the stress-strain curve of cylindrical specimens and cubic specimens are basically consistent, but σ_c and peak strain (ε_P) of the stress-strain curve of cylindrical specimens are lower than those of the cubic specimens, and show more obvious brittleness characteristics. This also indicates that

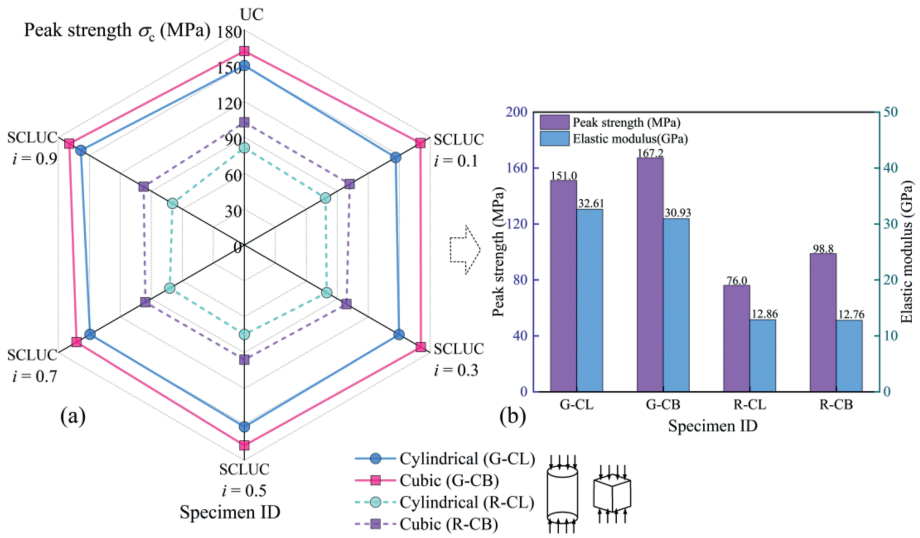

Fig. 6. Peak strength characteristics of cubic and cylindrical rock specimens in UC and SCLUC tests. (a) Peak strength of cubic and cylindrical specimens under different stress levels, (b) Average peak strength and elastic modulus characteristics of cubic and cylindrical specimens. Note: The elastic modulus data in Fig. 6b were sourced from Table 1.

the specimen's shape affects the mechanical behavior characteristics of rock, consistent with most research results (Brown and Hoek, 1980; Hawkins, 1998; Darlington et al., 2011; Al-Rkaby and Alafandi, 2015; Gong et al., 2022b; Yan et al., 2022). Additionally, compared with the red sandstone specimen material, the granite specimen material exhibited stronger brittle characteristics. For instance, the σ_c of G-CL specimen was higher than that of R-CL specimen, the ε_P was smaller than that of R-CL specimen, and the drop-off feature in the post-peak stage was more pronounced.

4.2. Peak strength characteristics

Based on the stress-strain curves, we further analyzed the σ_c characteristics of cylindrical and cubic specimens (Fig. 6). It can be seen that the σ_c of each type of rock specimen under UC and SCLUC tests is basically the same. This suggests that traditional UC and SCLUC tests do not significantly alter the mechanical characteristics of the rock. Additionally, it indicates that granite and red sandstone materials exhibit good homogeneity. Further statistics show that the average σ_c of G-CL specimen, G-CB specimen, R-CL specimen, and R-CB specimen are 151 MPa, 167.2 MPa, 76 MPa, and 98.8 MPa, respectively. The σ_c of G-CL specimens shows a 9.7 % reduction (16.18 MPa decrease) compared to G-CB specimens. Similarly, R-CB specimens exhibit a 23 % strength reduction (22.76 MPa decrease) relative to R-CL specimens. It can be inferred that the σ_c of cylindrical specimens is lower than that of cubic specimens. This is because during the loading process, the cube has a larger stress contact surface than the cylinder specimen, and the length/width ratio of the cube is 1:1 less than the length/diameter ratio of the cylinder is 2:1 (Hawkins, 1998; Ozkan et al., 2009; Tuncay and Hasancebi, 2009; Al-Rkaby and Alafandi, 2015; Meng et al., 2016; Quiñones et al., 2017; Chen et al., 2020; Yan et al., 2022). Furthermore, the σ_c of granite specimens is greater than that of red sandstone specimens. For instance, the σ_c of G-CB specimen is 69.3 % higher than that of R-CB specimen. This further corroborates the assertion made in Section 3.1 that granite exhibits more characteristics of hard rock brittleness compared to red sandstone materials.

4.3. Rockburst characteristics

The instantaneous rockburst failure process of the cylindrical (G-CL and R-CL) and cubic (G-CB and R-CB) specimens was recorded by using a high-speed camera, as shown in Figs. 7 and 8. Fig. 7a illustrates the critical instability rockburst failure process of G-CL specimen. It can be observed that prior to entering the rapid failure phase, there is bulging at the waist of the cylindrical specimen accompanied by minor fragment spalling. Subsequently, under continued loading, debris ejection occurs at the bulging portion of the cylindrical specimen's waist, leading swiftly into a rapid failure phase. The transition from entering the rapid failure phase to final failure lasted 2.88 s, indicating a relatively short overall failure duration. There was a significant dynamic ejection of numerous fragments, indicating rockburst characteristics. The post-failure G-CL specimen exhibits a V-shaped conjugate shear failure pattern (Fig. 8a). Compared with the G-CL specimen, the G-CB specimen also exhibits rockburst failure characteristics (Fig. 7b). It can be seen that when the G-CB specimen is loaded to a certain stage, it directly enters the rapid failure phase. The duration from entering the rapid failure phase to final failure was 4.4 s, during which the rapid failure phase from the initial to the telophase lasted 0.78 s. Dynamic ejection of a large amount of fragments occurred throughout the specimen (both upper and lower parts), and it was more pronounced, resulting in a split failure mode in G-CB specimens after failure (Fig. 8b). Overall, it can be inferred that the rockburst failure characteristics of G-CL and G-CB specimens are essentially similar and equally intense.

Fig. 7c and d illustrates the critical instability failure process of R-CL and R-CB specimens. It can be observed that both R-CL and R-CB specimens exhibit macroscopic failure cracks on their sides, and form an open configuration before entering rapid failure. With continued loading, instability failure occurs along the macroscopic cracks and open fractures of both R-CL and R-CB specimens. However, the overall rockburst failure characteristics are less severe compared to G-CL and G-CB specimens. For example, during the process of entering the rapid failure phase, the R-CL specimen only exhibits a minor amount of fragment ejection, showing failure characterized by large block spalling (Fig. 7c). The duration from

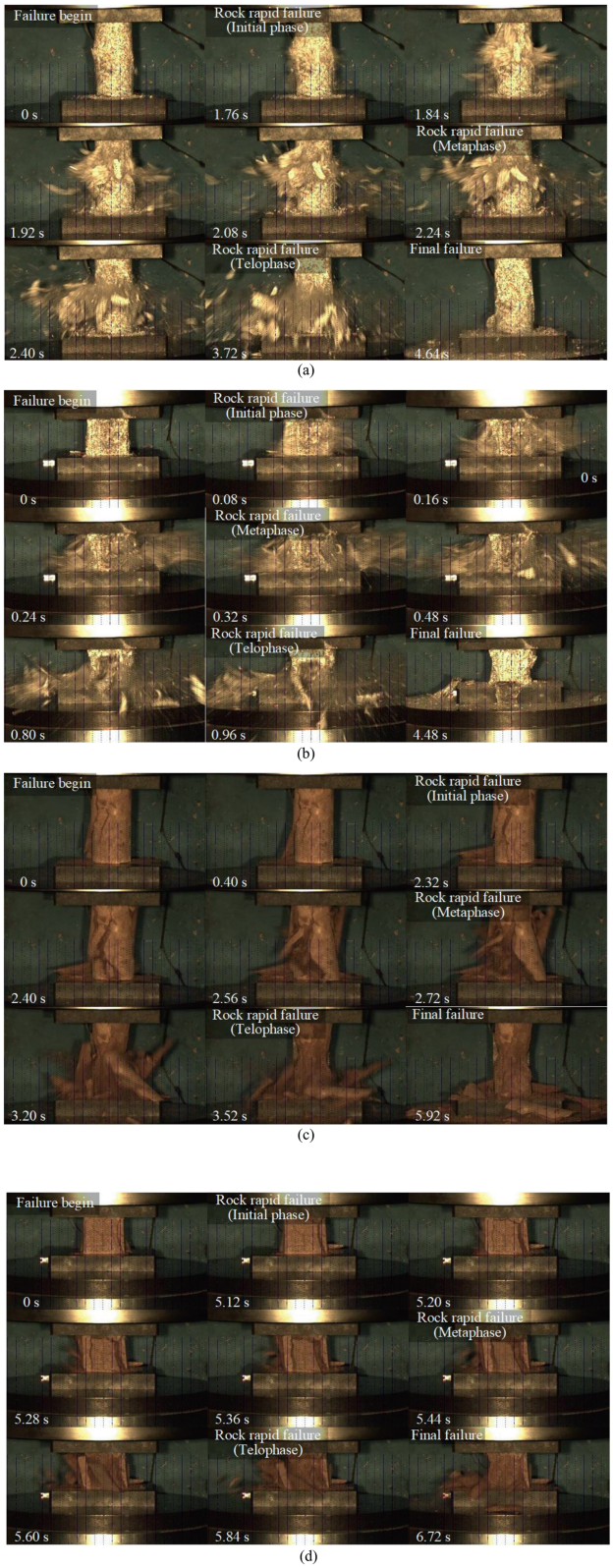

Fig. 7. Typical rockburst failure process of cylindrical and cubic specimens: (a) G-CL specimen (G-CL-0), (b) G-CB specimen (G-CB-0), (c) R-CL specimen (R-CL-0.7), and (d) R-CB specimen (R-CB-0.7). (Note: The initial time (0 s) is defined as the onset of macroscopic cracking, fragment detachment, or rapid failure on the specimen surface.)

entering the rapid failure phase to final failure lasted 3.6 s, with a relatively mild degree of rockburst, resulting in a conjugate shear failure after failure (Fig. 8c). Similarly, the rockburst failure characteristics of R-CB specimen are consistent with those of the R-CL specimen, both less severe (Fig. 7d). Although the duration from entering the rapid failure phase to final failure lasted only 1.6 s, the process of instability failure is accompanied by only a small amount of fragment ejection, indicating a relatively weak overall rockburst intensity. During the failure process of R-CB specimen, a significant amount of large block splitting fragments mainly parallel to the loading axis direction are generated, resulting in a split failure mode (Fig. 8d), with axial cracks extending through the entire axial height of the specimen. It is worth noting that although the duration from entering the rapid failure phase to final failure is short for R-CL and R-CB specimens during the rockburst failure process, their rockburst intense characteristics remain relatively weak. This is because they have already formed obvious macroscopic cracks and fractures before entering the rapid failure phase, leading to rapid failure after entering the failure phase and thereby shortening the duration of the rapid failure phase. Overall, the rockburst failure characteristics of R-CL and R-CB specimens are essentially similar and less severe compared to granite specimens. It can be inferred that the intense characteristics of rockburst failure are primarily governed by the rock material itself and are largely independent of the specimen shape.

4.4. W_{ET} of cylindrical and cubic rock specimens

Using the previously mentioned calculation methods of strain energy parameters (u_o^i, u_e^i, and u_d^i) and W_{ET}, we selected the loading-unloading curves of cylindrical and cubic rock specimens with an unloading stress level of 80 %–90 % (i.e. G-CL-0.9, G-CB-0.9, R-CL-0.9, and R-CB-0.9 specimens), and calculated the u_e and u_d, as well as W_{ET}. The calculation results are shown in Table 2.

From the calculation results, it can be observed that the W_{ET} index values of cylindrical and cubic specimens are identical. For instance, the W_{ET} of G-GL-0.9 and G-GB-0.9 specimens are 3.8. According to Eq. (10) of the W_{ET} discrimination index standard (Kidybiński, 1981), both are classified as having low rockburst proneness.

$$\left.\begin{array}{ll} W_{ET} > 5 & \text{High rockburst proneness} \\ 5 \geq W_{ET} \geq 2 & \text{Low rockburst proneness} \\ W_{ET} < 2 & \text{No rockburst proneness} \end{array}\right\} \quad (12)$$

The W_{ET} of R-GL-0.9 and R-GB-0.9 specimens are 1.9, indicating no rockburst proneness. Moreover, the physical critical rockburst failure characteristics recorded by high-speed cameras confirm this observation (Fig. 7). For example, both G-CL and G-CB specimens exhibit rockburst characteristics during the critical failure phase, with significant dynamic ejection of fragments, and a short duration of dynamic failure (Figs. 7a and b). However, compared to granite specimens, the overall rockburst failure characteristics of R-CL and R-CB specimens are weaker, with the destabilization process accompanied by only a small amount of fragment ejection, primarily presenting instability failure with large block detachment (Fig. 7c and d). This further demonstrates the fundamental consistency between W_{ET} assessments and the physical rockburst characteristics of rocks, supporting the rationality of using the W_{ET} to evaluate rockburst proneness. Additionally, the consistency of W_{ET} values between cylindrical and cubic specimens suggests that the shape of specimens has no influence on the W_{ET}. It should be noted that whether the W_{ET} calculated at unloading stress levels of 80 %–90 % reflects the strain energy of the rock at the peak strength point still requires further proof. These points will be discussed in the later chapters.

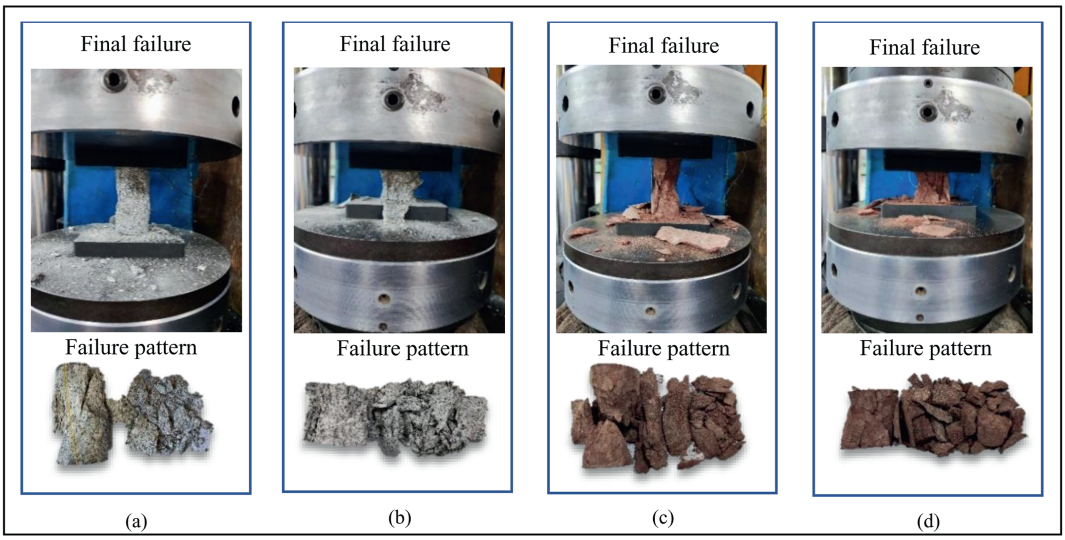

Fig. 8. Final failure pattern of cylindrical and cubic specimens after rockburst (see Fig. 7). (a) G-CL specimen, (b) G-CB specimen, (c) R-CL specimen; and (d) G-CB specimen.

Table 2
Calculation of the W_{ET} index of cubic and cylindrical rock specimens.

Specimen ID	Actual unloading level	u_e (mJ/mm^3)	u_d (mJ/mm^3)	W_{ET}	Determination of rockburst proneness
G-CL-0.9	90 %	0.2564	0.0673	3.81	Low
G-CB-0.9	88 %	0.2867	0.0756	3.79	Low
R-CL-0.9	94 %	0.1378	0.0721	1.91	No
R-CB-0.9	94 %	0.2341	0.123	1.90	No

5. Verification of the migration effect of W_{ET} in cylindrical and cubic rock specimens

5.1. Verification of the rationality of W_{ET} using the linear energy storage law

Fig. 9 illustrates the LES and LED laws of cylindrical (G-CL and R-CL) and cubic (G-CB and R-CB) rock specimens. It can be observed that the coefficient of determination (R^2) for the fitted results ranges from 0.9934 to 0.9997, indicating a strong linear relationship between u_e^i, u_d^i, and u_o^i for both cylindrical and cubic specimens. Furthermore, it is evident that the data fitting curves for the strain energy parameters of cylindrical and cubic specimens overlap (Fig. 9a and c), suggesting a similar energy storage capacity characteristic between cylindrical and cubic rock specimens. For instance, by analyzing the fitting functions of granite specimens, the A for G-CL specimens and G-CB specimens are 0.7983 and 0.7917, respectively (Fig. 9a), indicating essentially similar energy storage capacity characteristics. Furthermore, by concurrently fitting the strain energy parameter data of G-CL and G-CB specimens, it is found that all data points lie on a straight line, with the A being 0.79 (Fig. 9b), further demonstrating that the shape of the specimens has no effect on the energy storage capacity of rock materials. Similarly, the A for R-CL and R-CB specimens are 0.6622 and 0.66, respectively (Fig. 9c). Meanwhile, the concurrent fitting of the strain energy parameter data of R-CL and R-CB specimens yields an A value of 0.66 (Fig. 9d), suggesting once again that the specimen shape has no effect on the energy storage capacity of rock material. Additionally, it is noteworthy that the A for granite specimens is greater than that for red sandstone specimens, consistent with the previously mentioned σ_c and physical rockburst failure characteristics. In summary, the consistency of the A between cylindrical and cubic specimens confirms that the shape of the specimens does not affect the energy storage capacity of rock materials. Simultaneously, the LES law of rock materials also provides theoretical support for the application of W_{ET} on cylindrical and cubic specimens. Therefore, the rationality of W_{ET} migration from cubic to cylindrical is confirmed from a theoretical and quantitative perspective.

5.2. Independence of W_{ET} and W_{ET}^P from cylindrical and cubic rock specimen shape

To further analyze and verify the migration effect of W_{ET} between cylindrical and cubic rock specimens, as well as to investigate whether there are differences between W_{ET} and W_{ET}^P under cylindrical and cubic rock specimens, we calculated W_{ET}^P for G-CL, G-CL, R-CL, and R-CB specimens using Eqs. (6)–(8). The calculation results are depicted in Fig. 10. Meanwhile, Fig. 10 contains the theoretical function curves of Eq. (3) and ideal function curves of Eq. (4) for G-CL, G-CL, R-CL, and R-CB specimens, as well as the W_{ET}.

It can be observed from Fig. 10 that the ideal function curve of Eq. (4) is a straight line, with its value equal to $A/(1-A)$. However, the theoretical function curve of Eq. (3), due to the presence of the constant term b, causes the ratio of elastic strain energy to dissipated strain energy to first rise and then stabilize with increasing input strain energy. After stabilization, the theoretical curve aligns with the ideal curve of energy storage-dissipation ratio. It is worth noting that the data points of W_{ET} at the unloading level of 80 %–90 % and W_{ET}^P at peak strength for cylindrical and cubic rock specimens are either on or close to the ideal straight line and theoretical curve. This indicates that the W_{ET} and W_{ET}^P values for cylindrical and cubic specimens are essentially consistent and independent of specimen shape. Meanwhile, the evaluation of rockburst proneness for the cylindrical and cubic specimens also

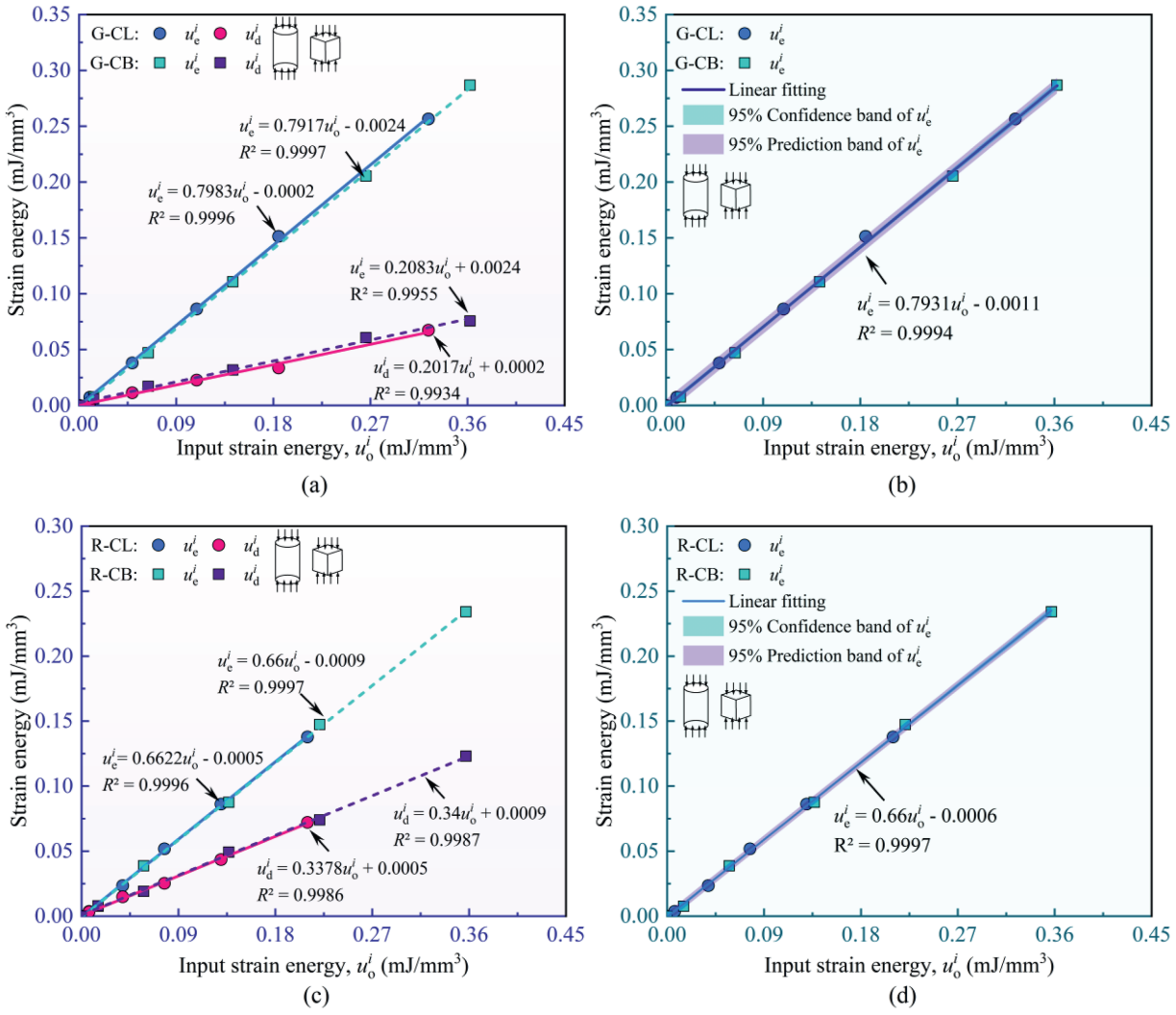

Fig. 9. Linear energy storage and dissipation laws of cylindrical and cubic specimens: (a) G-CL specimens, (b) G-CB specimens, (c) R-CL specimens, and (d) G-CB specimens.

confirmed this. For example, cylindrical and cuboid specimens of red sandstone exhibit no rockburst proneness, whereas granite exhibits low rockburst proneness. It is validated from an energy theory perspective that the evaluation values of W_{ET} and W_{ET}^P are essentially consistent. Combining the above analysis, the migration effect of W_{ET} and W_{ET}^P between cylindrical and cubic specimens is confirmed, which corresponds to the theoretical verification in Section 2. This indicates that the calculation of W_{ET} and W_{ET}^P is not affected by the shape of cylindrical and cubic rock specimens, i.e. the W_{ET} and W_{ET}^P are independent of the specimen shape effects.

6. Discussion

6.1. Stability of W_{ET}^P with respect to W_{ET}

According to the results discussed above, the independence of W_{ET} and W_{ET}^P from specimen shape effects using the LES law was confirmed. In addition, from the trend observed in the ideal curve (Fig. 10) of energy storage-dissipation based on the LES law, it is evident that W_{ET}^P is more stable than W_{ET}. It can be observed from the distribution of W_{ET} and W_{ET}^P data points that W_{ET} converges to W_{ET}^P. The W_{ET}^P data for six specimens of the same specimen shape are stable and closely match the ideal curve plotted for energy storage-dissipation ratio, indicating that the ratio of u_e^i to u_d^i stabilizes to a fixed value at the peak. In addition to the experimental data mentioned above, we also selected data from four other types of rocks (fine granite, green sandstone, yellow granite, and white marble) to verify the stability of W_{ET}^P (Gong et al., 2019a). Similar to the experimental data mentioned above, the W_{ET} data for the other four rocks are located on or close to the theoretical curve of energy storage-dissipation ratio and converge to W_{ET}^P. The W_{ET}^P data for the six specimens of each rock are also stable and closely follow the ideal energy storage-dissipation ratio curve (Fig. 11). Additionally, we observed that the W_{ET} data for some rocks did not converge to the ideal energy storage-dissipation ratio curve. This deviation is due to the influence of the fitting constant b in the LES law of the rocks. As described in Section 5.2, the constant b affects the characteristics of the theoretical energy storage-dissipation ratio curve. According to the theoretical Eq. (3) for the energy storage-dissipation ratio described in Section 2, the energy storage-dissipation ratio is primarily related to the rock's A, u_o^i, and b. Although it has been shown that the value of b differs from the A by three orders of magnitude (Fig. 9). However, when the u_o^i value

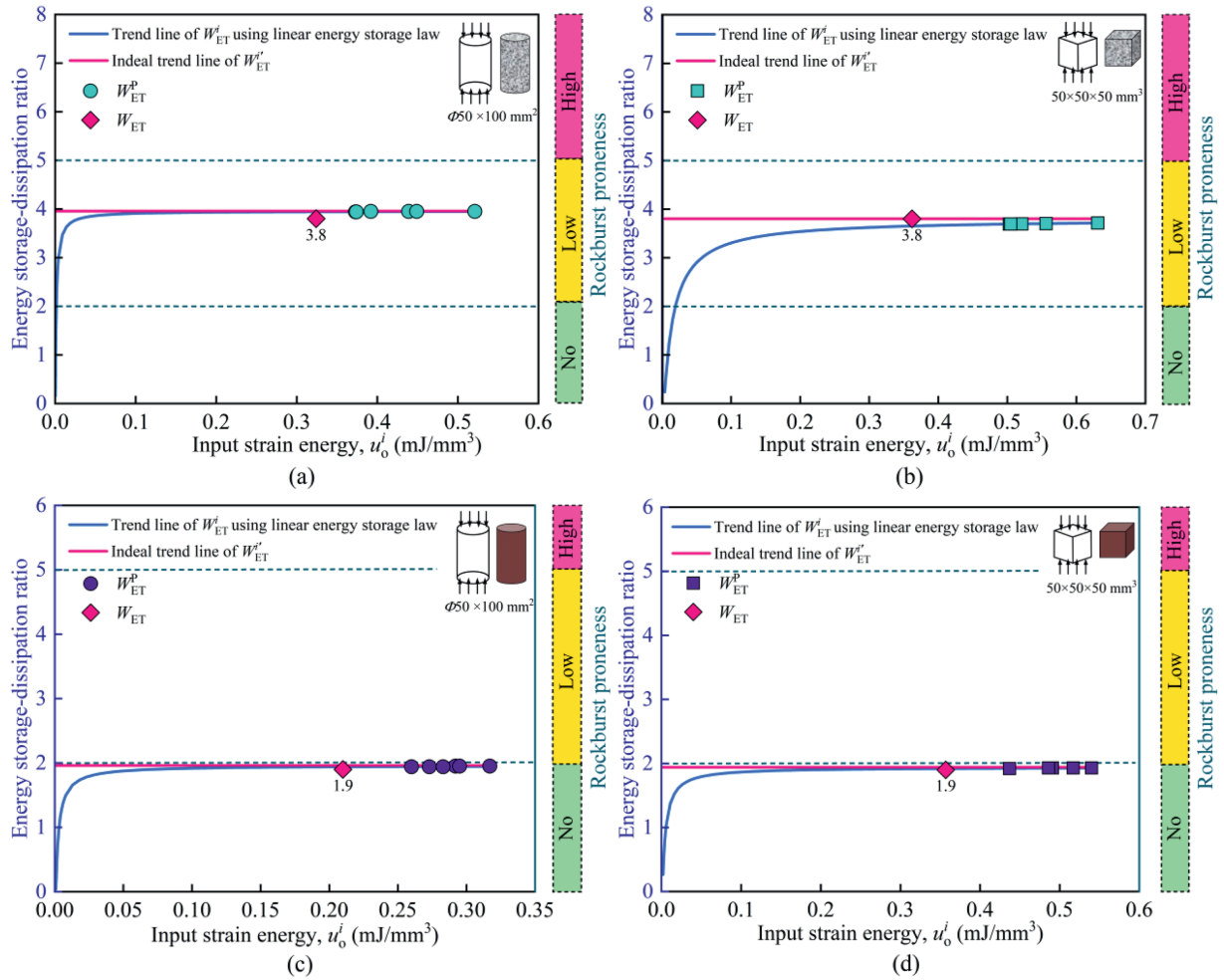

Fig. 10. Energy storage-dissipation ratio of cylindrical and cubic specimens: (a) G-CL specimens, (b) G-CB specimens, (c) R-CL specimens, and (d) R-CB specimens.

is very low, the product of the A and the u_o^i is also minimal. In this case, the value of b significantly impacts the theoretical energy storage-dissipation ratio. As the input energy increases, the product of the A and u_o^i also rises, and once it reaches a certain level, the influence of b on elastic strain energy and dissipated strain energy becomes negligible. At this point, the theoretical energy storage-dissipation ratio curve almost converges with the ideal energy storage-dissipation ratio curve. The W_{ET}^{P} data for the rocks, which consistently align with the ideal energy dissipation ratio curve, suggest that they are largely unaffected by the value of b. In contrast, the W_{ET} data for some rocks are influenced by b. This also further confirms that W_{ET}^{P} can more reliably reflect the elastic energy at the rock peak point than W_{ET}.

Additionally, the concept of coefficient of variation (CV) is introduced to quantitatively investigate the differences in W_{ET}^{P}, peak strength, density, and P-wave velocity data for six specimens prepared from the same rock type. The CV is a dimensionless coefficient used to compare the dispersion of data. It is defined as follows:

$$CV = \frac{SD}{MN} \times 100\% \tag{13}$$

where SD and MN denote the standard deviation and the mean, respectively. The results are shown in Fig. 12. Compared with the CV values of peak strength, density, and P-wave velocity, the CV of W_{ET}^{P} data was much smaller, suggesting that the W_{ET}^{P} data has little variation. In other words, W_{ET}^{P} reflects the relative magnitude of energy storage and dissipation during the entire pre-peak loading stage of rock, making it more suitable for characterizing the rock's energy storage capacity. Overall, based on experimental results and theoretical reasoning, W_{ET}^{P} is more stable compared to W_{ET}. Therefore, W_{ET}^{P} can be satisfactorily used as a substitute index for W_{ET} in evaluating the rockburst proneness of rock.

6.2. Limitations and suggestions

In this study, based on the theoretical deduction and experimental verification, it is proved that the W_{ET} and W_{ET}^{P} are independent of the specimen shape effects. It also proves that W_{ET}^{P} is more stable than W_{ET}. However, it should be pointed out that W_{ET} and W_{ET}^{P} only reflect the ratio of elastic strain energy to dissipated strain energy before peak strength, representing only the relative magnitudes of elastic strain energy and dissipated strain energy. They cannot directly reflect the absolute energy state of rockburst potential, and cannot characterize the absolute kinetic energy when rockburst occurs. Additionally, it should be noted that this paper only analyzed and discussed the characteristics of W_{ET} and W_{ET}^{P} using cylindrical and cubic specimens. Furthermore, if conditions permit, it is recommended to use standard Φ50

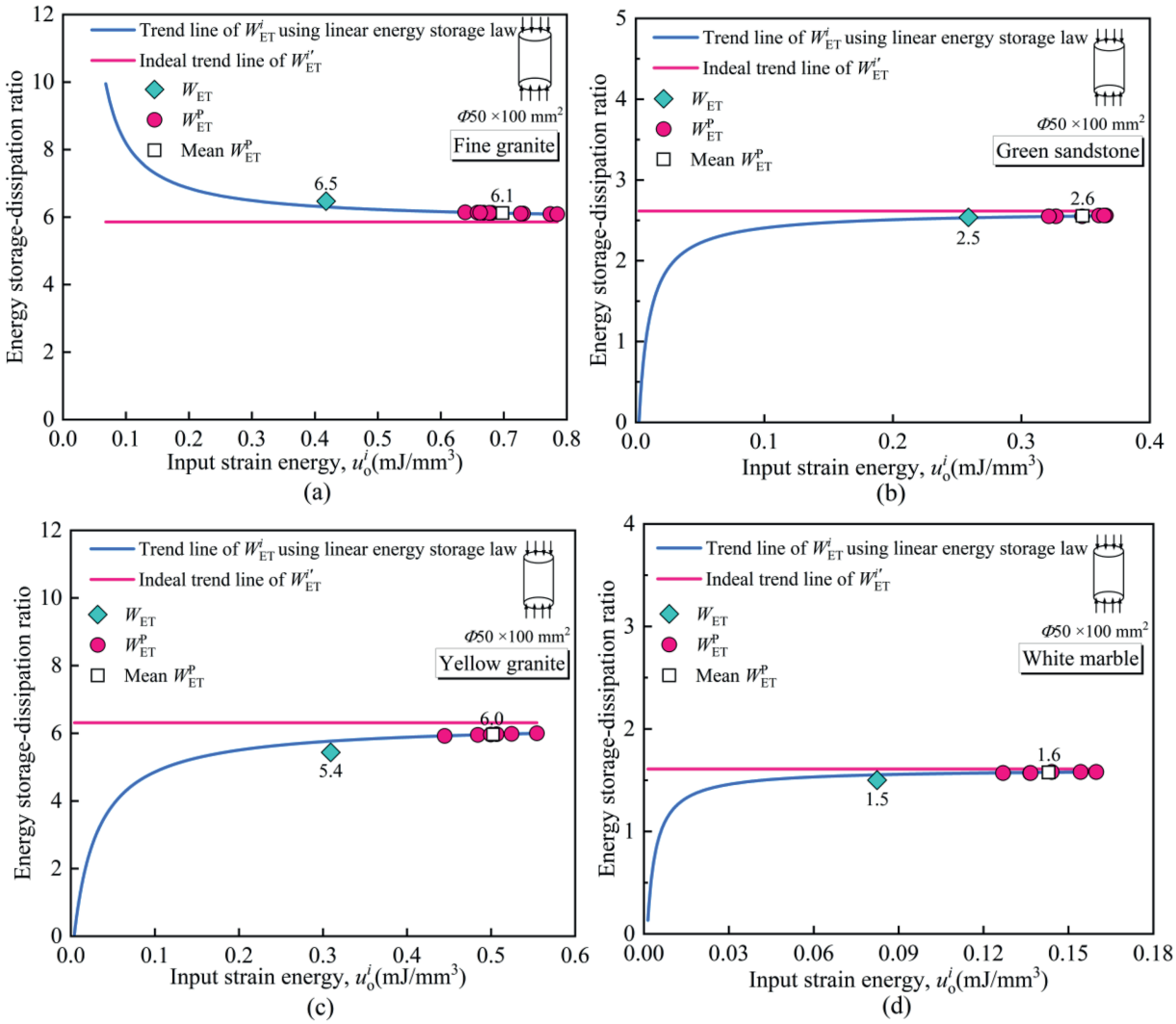

Fig. 11. Variations in energy storage-dissipation ratio with input strain energy: (a) Fine granite, (b) Green sandstone, (c) Yellow granite, and (d) White marble (Note: Data were sourced from Gong et al., 2019a).

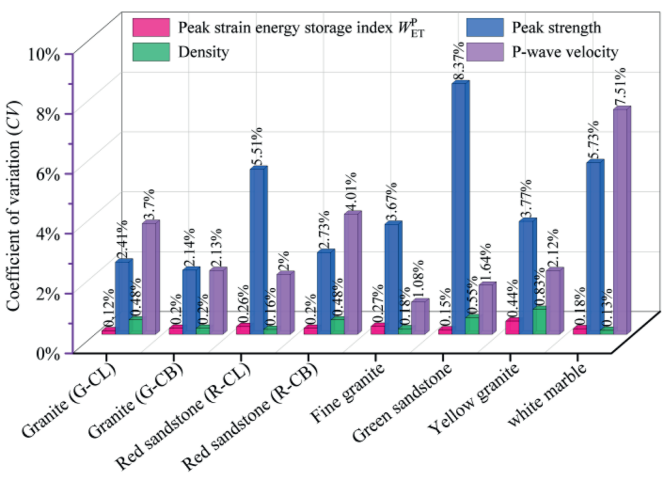

Fig. 12. Coefficient of variation (*CV*) values for peak-strength strain energy storage index, peak strength, density, and P-wave velocity across eight rock types (Note: Data for fine granite, green sandstone, yellow granite, and white marble were sourced from Gong et al., 2019a).

mm × 100 mm cylinder rock specimens to calculate W_{ET} and W_{ET}^{P}, as they are easy to specimen and process on-site. Moreover, from the evaluation results of the W_{ET} and W_{ET}^{P}, it is convenient to compare with the evaluation results of other rockburst proneness indicators.

7. Conclusions

In this study, based on the LES law of rock, the influence of specimen shape effect on W_{ET} was discussed from theoretical analysis and experimental verification. The main conclusions are as follows:

(1) The independence of W_{ET} from the specimen shape effect was theoretically derived using the LES law. The W_{ET} is directly related to the energy storage coefficient (A) of rock materials.
(2) The experimental results verified that the mechanical behavior characteristics of rock were affected by the shape of cylindrical and cubic specimens, while W_{ET} and A of rock

specimens were opposite. The W_{ET} values of cylindrical and cubic rock specimens closely approximate the theoretical value of the energy storage-dissipated ratio predicted by the LES law. Hence, the migration effect of W_{ET} in cylindrical and cubic rock specimens is proved using the LES law.

(3) The W_{ET} and W_{ET}^{P} are independent of specimen shape effects. In addition to theoretical verification that the W_{ET} independent of the specimen shape effects, the experimental consistency of W_{ET} values and rockburst proneness between cylindrical and cuboid specimens further supports this finding.

(4) The W_{ET} values converging to W_{ET}^{P}, and W_{ET}^{P} is more stably distributed near the ideal energy storage-dissipation ratio curve than W_{ET}. Thus, W_{ET}^{P} can be satisfactorily used as a substitute index for W_{ET} in evaluating the rockburst proneness of rock.

CRediT authorship contribution statement

Zhichao He: Methodology, Investigation, Validation, Formal analysis, Data curation, Writing – original draft. **Fengqiang Gong:** Conceptualization, Supervision, Writing – review & editing, Funding acquisition. **Li Ren:** Writing – review & editing, Supervision, Resources, Formal analysis. **Da Huang:** Writing – review & editing, Data curation, Formal analysis. **Weimin Yang:** Writing – review & editing, Formal analysis.

Declaration of competing interest

The authors declare that they have no known competing financial interests or personal relationships that could have appeared to influence the work reported in this paper.

Acknowledgments

We acknowledge the funding support from the National Natural Science Foundation of China (Grant No. 42077244), the State Key Laboratory of Intelligent Construction and Healthy Operation and Maintenance of Deep Underground Engineering, Sichuan University (Grant No. SDGZK2431), and the Postgraduate Research & Practice Innovation Program of Jiangsu Province (Grant No. KYCX24_0434).

References

Afraei, S., Shahriar, K., Madani, S.H., 2018. Statistical assessment of rock burst potential and contributions of considered predictor variables in the task. Tunn. Undergr. Space Technol. 72, 250–271.

Ahmad, M., Katman, H.Y., Al-Mansob, R.A., et al., 2022. Prediction of rockburst intensity grade in deep underground excavation using adaptive boosting classifier. Complexity (1), 6156210.

Al-Rkaby, A.H., Alafandi, Z.M., 2015. Size effect on the unconfined compressive strength and modulus of elasticity of limestone rock. Electron. J. Geotech. Eng. 20, 1393–1401.

Askaripour, M., Saeidi, A., Rouleau, A., et al., 2022. Rockburst in underground excavations: a review of mechanism, classification, and prediction methods. Undergr. Space 7 (4), 577–607.

Bacha, S., Long, Z.M., Javed, A., et al., 2020. A review of rock burst's experimental progress, warning, prediction, control and damage potential measures. J. Min. Environ. 11 (1), 31–48.

Brauner, G., 1994. Rockburst in Coal Mines and Their Prevention. Balkema A A, Netherland.

Brown, E., Hoek, E., 1980. Underground Excavations in Rock. CRC Press, London, UK.

Cai, M.F., 2016. Prediction and prevention of rockburst in metal mines–A case study of sanshandao gold mine. J. Rock Mech. Geotech. Eng. 8, 204–211.

Chen, Z.H., Huang, L.Q., Li, X.B., et al., 2020. Influences of the height to diameter ratio on the failure characteristics of marble under unloading conditions. Int. J. GeoMech. 20, 04020148.

Cook, N.G.W., 1963. The basic mechanics of rockbursts. J. S. Afr. Inst. Min. Metall 64 (3), 71–81.

Darlington, W.J., Ranjith, P.G., Choi, S.K., 2011. The effect of specimen size on strength and other properties in laboratory testing of rock and rock-like cementitious brittle materials. Rock Mech. Rock Eng. 44, 513–529.

Dai, J.H., Gong, F.Q., Huang, D., et al., 2025. Quantitative evaluation method of rockburst prevention effect for anchoring rock masses around deep-buried tunnels. Tunn. Undergr. Space Technol. 156, 106268.

Dong, L.J., Li, X.B., Peng, K., 2013. Prediction of rockburst classification using random forest. T. Nonferr. Metal. Soc. 23, 472–477.

Feng, X.T., Pei, S.F., Jiang, Q., et al., 2017. Deep fracturing of the hard rock surrounding a large underground cavern subjected to high geostress: in situ observation and mechanism analysis. Rock Mech. Rock Eng. 50, 2155–2175.

Gong, F.Q., Dai, J.H., Xu, L., 2023. A strength-stress coupling criterion for rockburst: inspirations from 1114 rockburst cases in 197 underground rock projects. Tunn. Undergr. Space Technol. 142, 105396.

Gong, F.Q., Luo, S., Jiang, Q., Xu, L., 2022a. Theoretical verification of the rationality of strain energy storage index as rockburst criterion based on linear energy storage law. J. Rock Mech. Geotech. 14, 1737–1746.

Gong, F.Q., Ni, Y.X., Jia, H.Y., 2022b. Effects of specimen size on linear energy storage and dissipation laws of red sandstone under uniaxial compression. Bull. Eng. Geol. Environ. 81, 386.

Gong, F.Q., Ni, Y.X., Ren, L., 2022c. Effects of loading rate on rockburst proneness of granite from energy storage and surplus perspectives. Rock Mech. Rock Eng. 55, 6495–6516.

Gong, F.Q., Wang, Y.L., Luo, S., 2020. Rockburst proneness criteria for rock materials: review and new insights. J. Cent. South Univ. 27, 2793–2821.

Gong, F.Q., Yan, J.Y., Li, X.B., et al., 2019a. A peak-strength strain energy storage index for rock burst proneness of rock materials. Int. J. Rock Mech. Min. Sci. 117, 76–89.

Gong, F.Q., Yan, J.Y., Luo, S., et al., 2019b. Investigation on the linear energy storage and dissipation laws of rock materials under uniaxial compression. Rock Mech. Rock Eng. 52, 4237–4255.

Hawkins, A.B., 1998. Aspects of rock strength. Bull. Eng. Geol. Environ. 57, 17–30.

He, Z.C., Gong, F.Q., Wu, W.X., et al., 2021a. Experimental investigation of the mechanical behaviors and energy evolution characteristics of red sandstone specimens with holes under uniaxial compression. Bull. Eng. Geol. Environ. 80, 5845–5865.

He, Z.C., Gong, F.Q., Luo, S., 2021b. Evaluation of the rockburst proneness of red sandstone with prefabricated boreholes: an experimental study from the energy storage perspective. Geomat. Nat. Hazards Risk 12, 2117–2154.

He, M.C., Cheng, T., Qiao, Y.F., et al., 2023. A review of rockburst: experiments, theories, and simulations. J. Rock Mech. Geotech. 15, 1312–1353.

He, Z.C., Gong, F.Q., Gao, M.Z., 2025a. Experimental study on the mechanical behavior of high-stress rocks during real-time drilling. Int. J. Coal. Sci. Tech. 12 (1), 37.

He, Z.C., Gong, F.Q., Ren, L., et al., 2025b. Energy relief effect of real-time drilling to prevent rockburst in high-stress rock. J. Rock Mech. Geotech. Eng. https://doi.org/10.1016/j.jrmge.2025.04.030.

Keneti, A., Sainsbury, B.A., 2018. Review of published rockburst events and their contributing factors. Eng. Geol. 246, 361–373.

Khan, N.M., Ahmad, M., Cao, K., Ali, I., Liu, W., Rehman, H., Ahmed, T., 2022. Developing a new bursting liability index based on energy evolution for coal under different loading rates. Sustainability 14 (3), 1572.

Kidybiński, A., 1981. Bursting liability indices of coal. Int. J. Rock Mech. Min. Sci. 295–304.

Klammer, A., Peintner, C., Gottsbacher, L., Biermann, J., Blümel, M., Schubert, W., Marcher, T., 2023. Investigation of the influence of grain-scale heterogeneity on strainburst proneness using rock-like material. Rock Mech. Rock Eng. 56 (1), 407–425.

Leveille, P., Sepehri, M., Apel, D.B., 2017. Rockbursting potential of kimberlite: a case study of Diavik diamond mine. Rock Mech. Rock Eng. 50 (12), 3223–3231.

Li, N., Jimenez, R., 2018. A logistic regression classifier for long-term probabilistic prediction of rock burst hazard. Nat. Hazards 90, 197–215.

Luo, S., Gong, F.Q., 2022. Evaluation of rockburst proneness considering specimen shape by storable elastic strain energy. Deep undergr. Sci. Eng. 1, 116–130.

Li, J.M., Tang, S.B., Li, T.J., et al., 2025b. Study on rockburst control of deep-buried tunnel by combining advanced stress release borehole and hydraulic fracturing. Tunn. Undergr. Space Technol. 160, 106517.

Li, J.M., Tang, S.B., Zhang, J.L., et al., 2025a. Multitask intelligent early warning of rockbursts based on classification-regression cascaded network model. Int. J. Rock Mech. Min. Sci. 189, 106103.

Luo, Y., Huang, J.C., Si, X.F., et al., 2025. An energy-based method for uniaxially compressed rocks and its implication. J. Rock Mech. Geotech. Eng. 17 (3), 1429–1444.

Malki, J., Vennes, I., Rowe, C.D., Mitri, H.S., 2025. Evaluation of rock burstability with mechanical property testing and microscopic image analysis. Rock Mech. Rock Eng. 58, 4441–4457.

Meng, Q.B., Zhang, M.W., Han, L.J., Pu, H., Li, H., 2016. Effects of size and strain rate on the mechanical behaviors of rock specimens under uniaxial compression. Arabian J. Geosci. 9, 527.

Neyman, B., Szecowka, Z., Zuberek, W., 1972. Effective methods for fighting rock bursts in Polish collieries. In: Proceedings of the 5th International Strata Control Conference, pp. 23–31.

Ozkan, I., Ozarslan, A., Genis, M., Ozsen, H., 2009. Assessment of scale effects on uniaxial compressive strength in rock salt. Environ. Eng. Geosci. 15, 91–100.

Panthi, K.K., 2012. Evaluation of rock bursting phenomena in a tunnel in the himalayas. Bull. Eng. Geol. Environ. 71, 761–769.
Peng, S.S., 1978. Coal Mine Ground Control. Wiley, New York, USA.
Qu, H.L., Yang, L.H., Zhu, J.B., et al., 2022. A multi-index evaluation method for rockburst proneness of deep underground rock openings with attribute recognition model and its application. Int. J. Rock Mech. Min. Sci. 159, 105225.
Quiñones, J., Arzúa, J., Alejano, L.R., et al., 2017. Analysis of size effects on the geomechanical parameters of intact granite samples under unconfined conditions. Acta Geotech 12, 1229–1242.
Ran, Q.C., Liang, Y.P., Yang, Z.L., et al., 2025a. Deterioration mechanisms of coal mechanical properties under uniaxial multi-level cyclic loading considering initial damage effects. Int. J. Rock Mech. Min. Sci. 186, 106006.
Ran, Q.C., Liang, Y.P., Zou, Q.L., et al., 2025b. Failure mechanisms of sandstone subjected to cyclic loading considering stress amplitude effects. Int. J. Coal. Sci. Techn. 12, 66.
Sepehri, M., Apel, D.B., Adeeb, S., et al., 2020. Evaluation of mining-induced energy and rockburst prediction at a diamond mine in Canada using a full 3D elastoplastic finite element model. Eng. Geol. 266, 105457.
Shan, Z.G., Yan, P., 2010. Management of rock bursts during excavation of the deep tunnels in jinping II hydropower station. Bull. Eng. Geol. Environ. 69, 353–363.
Singh, S., 1988. Burst energy release index. Rock Mech. Rock Eng. 21, 149–155.
Si, X.F., Zhang, Z.L., Li, X.B., et al., 2025. Influences of maximum principal stress direction and cross-section shape on tunnel stability. J. Rock Mech. Geotech. Eng. 17 (4), 2159–2180.
Stewarski, E., 1987. Energetic indicator of liability of rocks to bursts determined during shock loading with Hopkin's bar. Stanislaw Staszic Acad. Min. Metall. Crackow, Min. Bull. 129, 263–269.
Su, C.D., Yuan, R.F., Zhai, X.X., 2013. Experimental research on bursting liability index of coal samples of chengjiao coal mine. Chin. J. Rock Mech. Eng. 32 (S2), 3696–3704 (in Chinese).
Szecowka, Z., Domzal, J., Ozana, P., 1973. Energy Index of Natural Bursting Ability of Coal. Transactions of the Central Mining Institute. No. 594.
Tan, Y.A., 1992. Discussion on the energy impact index of rockburst. Hydrogeol. Eng. Geol. 19, 10–12.
Tuncay, E., Hasancebi, N., 2009. The effect of length to diameter ratio of test specimens on the uniaxial compressive strength of rock. Bull. Eng. Geol. Environ. 68, 491–497.
Wang, J.A., Park, H.D., 2001. Comprehensive prediction of rockburst based on analysis of strain energy in rocks. Tunn. Undergr. Space Technol. 16, 49–57.
Wang, W., Zhao, L., Pan, Y.S., et al., 2025. Evolution characteristics of an induced electric charge signal and identification method of charge for instability failure in loaded coal. J. Rock Mech. Geotech. Eng. 17 (7), 3973–3993.
Xiao, F.K., Shen, Z.L., Liu, G., Zhang, Z., Zhang, F.R., 2014. Relationship between hysteresis loop and elastoplastic strain energy during cyclic loading and unloading. Chin. J. Rock Mech. Eng. 33 (9), 1791–1797 (in Chinese).
Xie, H.P., Li, L.Y., Peng, R.D., et al., 2009. Energy analysis and criteria for structural failure of rocks. J. Rock Mech. Geotech. Eng. 1 (1), 11–20.
Xu, L., Gong, F.Q., Dai, J.H., et al., 2025a. Effects of bedding angles on rockburst proneness of layered anisotropic phyllites. J. Rock Mech. Geotech. Eng. 17 (7), 4288–4313.
Xu, L., Gong, F.Q., Ren, L., 2025b. Microwave irradiation power-induced energy evolution and rockburst failure characteristics in red sandstone. Eng. Fail. Anal. 181, 109899.
Xue, Y., Gao, F., Teng, T., et al., 2016. Effect of gas pressure on rock burst proneness indexes and energy dissipation of coal samples. Geotech. Geol. Eng. 34, 1737–1748.
Yan, J.Y., Gong, F.Q., Luo, S., 2022. Effects of length-to-diameter ratio on energy storage characteristics of rock materials under uniaxial compression. Bull. Eng. Geol. Environ. 81, 508.
Yang, X.H., Ren, T., Tan, L.H., et al., 2018. Developing coal burst propensity index method for Australian coal mines. Int. J. Min. Sci. Technol. 28, 783–790.
Zhang, P.L., Huang, L.Q., Li, X.B., 2025. Thermo-mechanical coupling damage constitutive relation of thermally treated rocks: statistical modeling and verification. Geomech Energy Envir 43, 100708.
Zhang, C.Q., Lu, J.J., Chen, J., Zhou, H., Yang, F.J., 2017. Discussion on rock burst proneness indexes and their relation. Rock Soil. Mech. 38, 1397–1404.
Zhao, Y.X., Jiang, Y.D., 2010. Acoustic emission and thermal infrared precursors associated with bump-prone coal failure. Int. J. Coal Geol. 83, 11–20.
Zhou, J., Li, X.B., Mitri, H.S., 2018. Evaluation method of rockburst: state-of-the-art literature review. Tunn. Undergr. Space Technol. 81, 632–659.
Zhou, K.P., Yun, L., Deng, H.W., Li, J.L., Liu, C.J., 2016. Prediction of rock burst classification using cloud model with entropy weight. T. Nonferr. Metal. Soc. 26, 1995–2002.

Fengqiang Gong obtained his BSc and MSc from Central South University (CSU), China, and PhD from CSU and Swiss Federal Institute of Technology in Lausanne (EPFL). He is a professor in School of Civil Engineering at Southeast University (SEU), a part-time professor at Hunan University of Science and Technology, and a guest professor at International Joint Research Laboratory of Henan Province for Underground Space Development and Disaster Prevention, China. His current research interests include failure mechanism of rockburst and spalling, rock energy storage law and application, rock dynamics, strength-weakening mechanism of deep rock, and damage constitutive model. He is a member of the editorial boards of *Geomechanics and Geophysics for Geo-Energy and Geo-Resources*, *Journal of Central South University*, *Acta Geophysica*, *Chinese Journal of Rock Mechanics and Engineering*, *Journal of Mining and Strata Control Engineering*, *Journal of Engineering Geology and Nonferrous Metals (Mining Section)*.